Nano Research
2020, 13(9): 2469–2477

ISSN 1998-0124 CN 11-5974/O4
https://doi.org/10.1007/s12274-020-2881-y

Research Article

Cobalt phosphide nanoarrays with crystalline–amorphous hybrid phase for hydrogen production in universal-pH

Hyunseok Yoon, Hee Jo Song, Bobae Ju, and Dong-Wan Kim (✉)

School of Civil, Environmental and Architectural Engineering, Korea University, Seoul 02841, Republic of Korea

Received: 1 April 2020 / **Revised:** 12 May 2020 / **Accepted:** 14 May 2020

ABSTRACT

To accomplish mass hydrogen production by electrochemical water-splitting, it is a necessary to develop robust, highly active, stable, and cost-effective hydrogen evolution reaction (HER) electrocatalysts that perform comparably to Pt in the universal pH range. In this work, cobalt phosphide hybrid nanosheets supported on carbon felt (CoP HNS/CF) are presented, which exhibit the superior electrocatalytic hydrogen production under a universal-pH. In these nanosheets, a single CoP HNS is composed of polycrystalline CoP and oxygen-enriched amorphous Co-O-P phase. Benefiting from its unique nanoarchitecture, as-fabricated CoP HNS/CF exhibits a tremendous electrocatalytic HER activity and outperforms Pt/C as well as state-of-the-art CoP electrocatalysts in universal-pH. In acidic and neutral media, the CoP HNS/CF shows superior electrocatalytic activity while maintaining its original hybrid crystalline-amorphous phase and morphology. In alkaline medium, the unexpected phase and morphological reorganization of CoP HNS/CF results in outstanding electrocatalytic operation. CoP HNS/CF not only achieves high electrocatalytic activity and kinetics, but also a stable and long operating lifetime even under a high current density of 500 mA·cm^{-2}. Furthermore, the fabrication of CoP HNS/CF can be scaled up easily, and the large CoP HNS/CF electrode also exhibits similar electrocatalytic activity and stability.

KEYWORDS

cobalt phosphide, self-supporting, electrocatalyst, hydrogen evolution reaction, universal-pH, large-scale

1 Introduction

Global warming and environmental pollution owing to the ever-increasing consumption of fossil fuels have become eminent concerns recently. So, it is now indispensable to develop alternative energy resources [1–4]. Molecular hydrogen (H_2) has been proposed as an ideal energy-transfer medium in the fields of transportation as well as stationary applications, due to its high gravimetric energy density (142 MJ·kg^{-1}) and carbon-emission free nature [1, 5–7]. So far hydrogen production by reforming natural gas has been considered as the most economical technique, however, electrochemical water-splitting combined with renewable energy resources is a potential pathway toward eco-friendly, sustainable and large-scale hydrogen production [6, 8–10]. Hydrogen production through water electrolysis primarily requires a highly active electrocatalyst to maximize the overall efficiency [1, 3, 5, 11]. Currently, platinum-on-carbon (Pt/C) is regarded as the most active electrocatalyst for the hydrogen evolution reaction (HER). However, its high cost and natural scarcity restrict its large-scale application [1, 4, 5].

In the past decade, considerable non-noble metal compounds have been researched to overcome these limitations. Among them, transition metal phosphides (TMPs) have been regarded as an attractive candidate for Pt-based electrocatalysts because of their low cost, good intrinsic activity, and stability toward HER in a wide pH range [5, 12, 13]. However, despite numerous efforts to develop TMPs for HER electrocatalysts, only few of them display comparable electrocatalytic activity to that of Pt-based electrocatalysts. Furthermore, these electrocatalysts even show inferior electrocatalytic performance in alkaline and neutral media [13–15]. Moreover, electrocatalysts are required to operate at high current densities (> 500 mA·cm^{-2}) in pursuit of industrialization [16, 17]. Therefore, it is highly desirable to explore robust, highly active, and stable HER electrocatalysts for the practical application of water electrolysis technology.

It is known that tailoring the composition, structure, or interface engineering of TMPs is an effective strategy to enhance the electrocatalytic activity. For example, doped or multi-metallic TMPs can optimize their electronic structure [18–20]; further, the nanoarchitecture can enlarge the reactive surface area [14, 21], and heterostructure can reduce the thermodynamic energy barrier [22, 23]. Moreover, electrocatalysts must have a strong adhesion to the current collector by preventing them from peeling off during the reaction for stability [14, 24]. Powder-type catalysts, however, cannot stand well under high current densities with robust gas evolution [25]. While, a self-supported structure can guarantee high stability due to the strong adhesion between the catalysts and substrates. Also, it can enlarge the electrochemically active surface area (ECSA), and even facilitate charge transfer [14, 26, 27]. In this regard, well-defined TMP nano-architectures that are self-supported on the current collector can provide a solution to realize the high-performance HER electrocatalyst even at high current densities.

Herein, we present the rational design of two-dimensional

Address correspondence to dwkim1@korea.ac.kr

(2D) ultrathin cobalt phosphide hybrid nanosheets (NSs) with a unique crystalline–amorphous phase supported on carbon felt substrate (CoP HNS/CF), which exhibits highly active and stable HER performance in universal-pH. Among various TMP compounds, we adopt CoP which is known for its excellent HER performance. For this, a precursor of $Co_2(OH)_2CO_3$ NS was directly constructed on a conducting substrate to induce the large exposure of reactive sites and effective attachment on the substrate. The hybrid crystalline–amorphous phase in a single NS was induced by adjusting the phosphidation time. Benefiting from the abundant exposure of ECSA, the CoP HNS/CF exhibited a high electrocatalytic HER performance in acidic and neutral media surpassing that of Pt/C at high current densities. In particular, the P leaching in the amorphous region during HER test in an alkaline medium generated the self-reorganization and formation of the CoP/$Co(OH)_2$ heterostructure on the substrate; this can promote the water-dissociation process, which results in an outstanding electrocatalytic HER performance in the alkaline medium. In addition, there was negligible degradation in HER performance after the stability tests even at a high current density of 500 mA·cm^{-2}. Finally, it was confirmed that the fabrication method of CoP HNS/CF can be scaled up easily regardless of substrate size. Furthermore, the large CoP HNS/CF electrode also exhibited comparable electrocatalytic performance to that of a small electrode.

2 Experimental

2.1 Synthesis of CoP HNS/CF

$Co_2(OH)_2CO_3$ NS/CF precursor was synthesized by a facile hydrothermal reaction process. Prior to the synthesis, commercial CF substrate was treated with UV-ozone for 30 min to make it hydrophilic. $Co(NO_3)_2{\cdot}6H_2O$ (0.1 M, 98%, Sigma-Aldrich) and urea (0.5 M, 99%, Samchun) were dissolved in deionized water (100–150 mL) under magnetic stirring for 30 min. This solution was transferred to a 200 mL Teflon-lined stainless-steel autoclave, together with the CF (exposed area: 1 cm × 1 cm or 4 cm × 4 cm), which stands vertically on ground, and hydrothermally reacted at 120 °C for 0–12 h. After the reaction, the substrate was washed and dried in an electronic oven. For phosphidation, $Co_2(OH)_2CO_3$ NS/CF precursor and NaH_2PO_2 (0.35 g) were placed at the center and in the upstream zone of a quartz tube, respectively, and heat-treated to 350 °C for 1–12 h with flowing Ar gas (20 sccm). CoP NW/CF was also synthesized through the phosphidation of $Co_2(OH)_2CO_3$ NW/CF precursor for 1.5 h.

2.2 Characterization

Scanning electron microscopy (SEM) images were obtained using a Hitachi SU-70 and COXEM CX-200. The Brunauer–Emmett–Teller (BET) specific surface area of the products was examined by a nitrogen adsorption–desorption process at 77 K using a Belsorp-mini II. X-ray diffraction (XRD) patterns were obtained with a Rigaku SmartLab or MiniFlex 600 using Cu Kα radiation. Surface chemical analysis was performed by X-ray photoelectron spectroscopy (XPS) (K-alpha+, Thermo Fisher Scientific). Transmission electron microscopy (TEM) analysis with Energy-dispersive X-ray spectroscopy (EDS) mapping was conducted using a JEOL JEM-2100F. Thermogravimetric analysis (TGA) was recorded on a Perlin-Elmer TGA-7 under an argon environment at a ramping rate of 5 °C·min^{-1}.

2.3 Electrochemical measurement

The HER electrocatalytic performance was evaluated in a three-electrode cell configuration using a potentiostat workstation (Ivium Technologies). The self-supported CoP HNS/CF and CoP NW/CF were directly employed as the working electrode (average loading mass: 1 mg·cm$^{-2}_{geo}$). In the case of Pt/C, a glassy carbon electrode (GCE, 5 mm in diameter) and a piece of carbon felt substrate loaded with Pt/C (0.2 mg·cm$^{-2}_{geo}$) were used as the working electrode (their electrocatalytic activities are shown in Fig. S1 in the Electronic Supplementary Material (ESM)). A graphite rod was used as the counter electrode and a saturated calomel electrode (SCE), Ag/AgCl electrode, and Hg/HgO electrode were used as the reference electrodes in the acidic, neutral, and alkaline media, respectively. 0.5 M H_2SO_4 (pH 0.3), 0.5 M phosphate buffer solution (PBS) (pH 7) and 1 M KOH (pH 14) were used as the electrolytes. Polarization curves were obtained using linear sweep voltammetry (LSV) at a scan rate of 5 mV·s^{-1}, at least three times to ensure the reliability of the results. All potentials were converted to the reversible hydrogen electrode (RHE) using the following equation: $E_{RHE} = E_{SCE} + 0.0591\times pH + 0.241$, $E_{Ag/AgCl} + 0.0591\times pH + 0.195$ or $E_{Hg/HgO} + 0.0591\times pH + 0.098$.

3 Results and discussion

The CoP HNS/CF was fabricated based on the hydrothermal reaction followed by controllable phosphidation steps, which is schematically illustrated in Fig. 1. CF was selected as the substrate and current collector. First, $Co_2(OH)_2CO_3$ NS precursor was grown on CF during the hydrothermal reaction at 120 °C for 12 h. Second, as-prepared $Co_2(OH)_2CO_3$ NS precursor was heat-treated with P source through a solid/gas phase reaction to form CoP HNS/CF. In addition, $Co_2(OH)_2CO_3$ nanowires (NWs) on CF ($Co_2(OH)_2CO_3$ NW/CF) precursor was also prepared when hydrothermally reacted for a short time, and CoP NW/CF was synthesized in the same phosphidation process.

The growth mechanism of $Co_2(OH)_2CO_3$ NS on CF substrate during the hydrothermal reaction was identified by SEM images (Figs. 2(a)–2(c) and Fig. S2 in the ESM). When the [$Co(NO_3)_2{\cdot}6H_2O$ + urea] solution in autoclave was heated to 120 °C, urea was decomposed and released ammonium, carbonate, and hydroxide ions into the solution. Then, cobalt ion was hydrolyzed and precipitated to form a uniform distribution of wire-shaped seed precipitations throughout the entire surface of the CF (Fig. S2(a) in the ESM). These seeds were grown up to one- dimensional (1D) NWs after reaction for 1.5 h (Fig. 2(b)) [28]. As the reaction was prolonged for

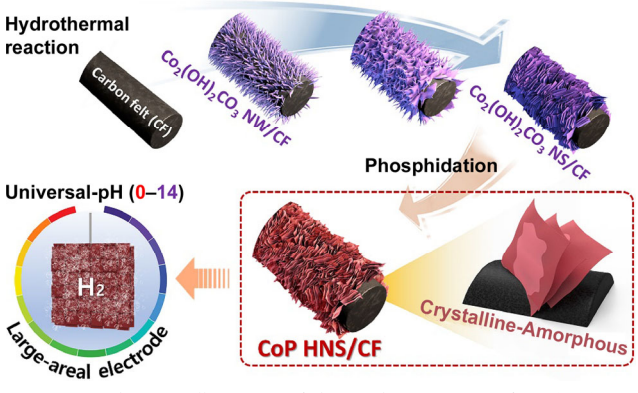

Figure 1 Schematic illustration of the synthetic process of $Co_2(OH)_2CO_3$ NS/CF precursor, CoP HNS/CF and the utilization of the electrodes for HER.

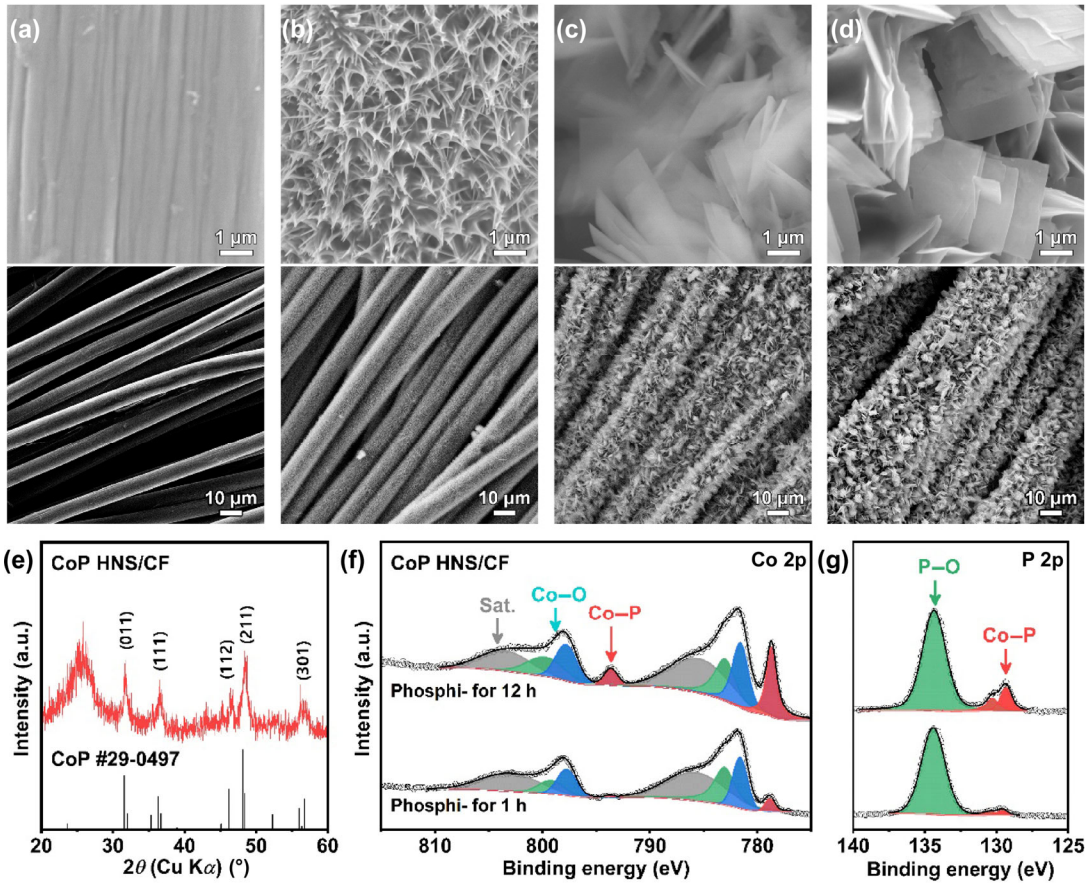

Figure 2 Synthesis of CoP HNS/CF. SEM images of (a) bare CF, (b) $Co_2(OH)_2CO_3$ NW/CF, (c) $Co_2(OH)_2CO_3$ NS/CF, and (d) CoP HNS/CF. (e) XRD pattern, (f) Co 2p and (g) P 2p XPS spectra of CoP HNS/CF.

3–6 h, additional products began to fill the gaps between the NWs, and the NWs gradually transformed into 2D sheets (Fig. S2(b) in the ESM). After reaction for 12 h, all NWs were transformed to NSs, where ultrathin NSs were close-packed but separated from each other (Fig. 2(c)). $Co_2(OH)_2CO_3$ NS/CF precursor was thermally reacted with PH_3 gas at 350 °C for 1 h to produce CoP HNS/CF. After phosphidation, CoP HNS still maintained their initial 2D morphology and well-attached to the CF substrate (Fig. 2(d)). The average size and thickness of CoP HNS is estimated to be about 2–3 μm and 30–40 nm, respectively. The nitrogen adsorption–desorption isotherms measured at 77 K are shown in Fig. S3 in the ESM. The BET specific surface area was estimated to be 3.57 $m^2 \cdot g^{-1}$.

The crystal information of $Co_2(OH)_2CO_3$ NW/CF, $Co_2(OH)_2CO_3$ NS/CF precursors, and CoP HNS/CF were characterized by XRD analysis (Fig. 2(e) and Fig. S4 in the ESM). All samples showed a broad peak at $2\theta \sim 26°$, which was attributed to the CF substrate. The XRD patterns of $Co_2(OH)_2CO_3$ NW/CF (corresponding to Fig. S4(a) in the ESM) and $Co_2(OH)_2CO_3$ NS/CF (corresponding to Fig. S4(b) in the ESM) were agreed well with those of hydrate $Co_2(OH)_2CO_3$ ($Co_2(OH)_2CO_3 \cdot xH_2O$) with an orthorhombic structure and dehydrated $Co_2(OH)_2CO_3$ with monoclinic structure, respectively, indicating dehydration of the precursor when $Co_2(OH)_2CO_3$ NW was transformed into $Co_2(OH)_2CO_3$ NS. After phosphidation, all reflected peaks in the pattern matched the CoP with orthorhombic structure without any secondary peaks (Fig. 2(e)), confirming that most of the $Co_2(OH)_2CO_3$ precursor was transformed to CoP. For the comparison of electrocatalytic HER performance, CoP NW/CF thermally phosphorized from $Co_2(OH)_2CO_3$ NW/CF at 350 °C for 1 h and CoP HNS/CF thermally phosphorized from $Co_2(OH)_2CO_3$ NS at 350 °C for 12 h were also prepared (Figs. S5 and S6 in the ESM).

The chemical states of CoP HNS/CF were characterized by XPS analysis. The survey spectrum of CoP HNS/CF showed the Co, P, and O bands corresponding to the CoP (Fig. S7 in the ESM). So, the high-resolution XPS spectra of Co 2p, P 2p and O 1s were investigated. The Co 2p spectrum showed four pairs of core-level peaks at 778.9/793.7, 781.6/797.8, 783.1/799.2, and 785.7/803.0 eV in the $2p_{3/2}/2p_{1/2}$ regions, respectively (Fig. 2(f)). The P 2p spectrum showed two core-level peaks at 129.6/130.5 eV in the lower binding energy region and another peak at 134.4 eV in the higher-binding-energy regions (Fig. 2(g)). The characteristic peaks at 778.9/793.7 eV for Co 2p and at 129.6/130.5 eV for P 2p represent Co-P binding and were in good agreement with a previously reported CoP structure [1, 3, 10, 11, 29]. Some peaks at 781.6/797.8 and 783.1/799.2 eV in Co 2p and at 134.4 eV in P 2p were attributed to Co–O and P–O binding, commonly due to the partial oxidization on the surface of CoP resulting from exposure to air [1, 8]. However, CoP HNS/CF phosphorized for 1 h exhibited weak Co-P binding intensity compared to those of CoP HNS/CF phosphorized for 12 h or previously reported CoP materials [1, 3, 10, 11, 29], implying that CoP HNS/CF phosphorized for 1 h possesses an O-rich CoP phase in its structure.

The detailed microstructures of the CoP HNS/CF were investigated by TEM analysis. Figure 3(a) and Fig. S8 in the ESM show the TEM images of the CoP HNS. Notably, there exist two distinct regions within a single CoP HNS particle: the rough section (section 1, orange color) and the other section (section 2, green color). The microstructures of these two sections were further investigated. Shown in the high-resolution TEM (HRTEM) image obtained from section 1

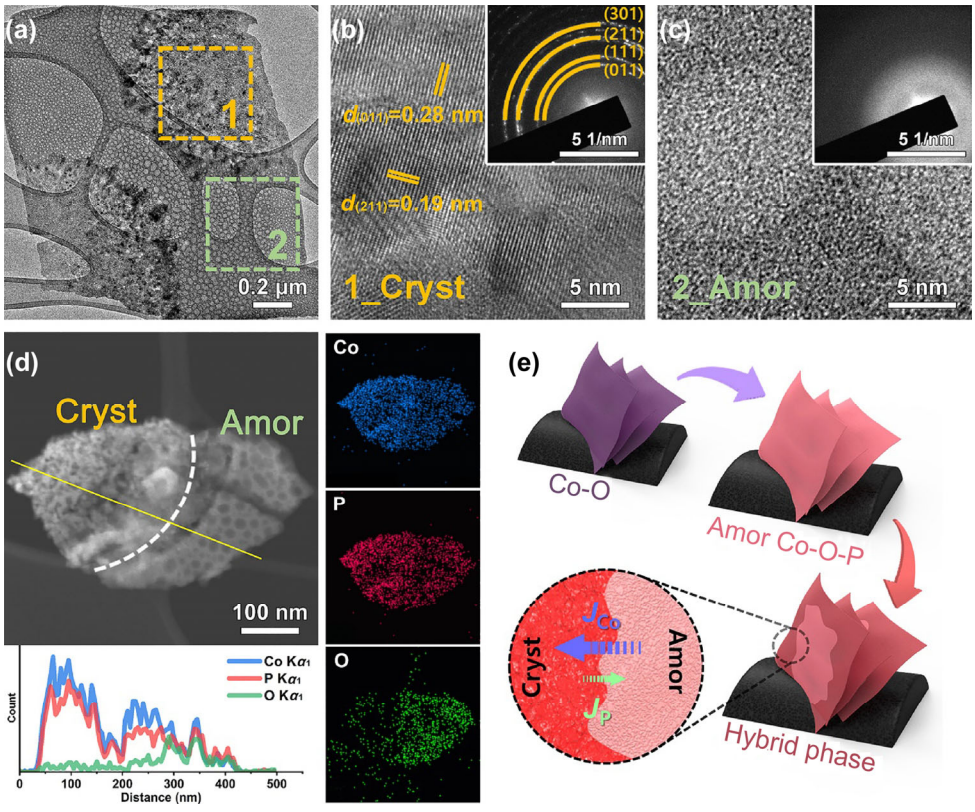

Figure 3 Microstructural information of CoP HNS/CF. (a) TEM image, (b) and (c) HRTEM images and SAED patterns taken from section 1 and section 2, respectively. (d) TEM-EDS elemental line-scanning and mapping of CoP HNS. (e) Schematic illustration for the formation of CoP HNS.

(Fig. 3(b)), the sheet was composed of nanopolycrystals, where their lattice fringes of 0.28 and 0.19 nm corresponded to the (011) and (211) planes of the CoP structure, respectively. In the selected area electron diffraction (SAED) pattern in section 1 (inset of Fig. 3(b)), four sets of ring patterns corresponding to the (011), (111), (211), and (301) planes of CoP could be observed clearly, which also confirms the formation of nanopolycrystalline CoP in section 1. In contrast, the HRTEM image and SAED pattern obtained from section 2 did not show any lattice fringes or distinct dot/ring patterns (Fig. 3(c)), indicating the amorphous phase in section 2. EDS elemental mapping under scanning TEM (STEM) analysis revealed that Co and P were located in both the crystalline and amorphous regions, whereas O was dominant only in the amorphous region (Fig. 3(d)). As expected in XPS analysis, CoP HNS possesses a significant amount of O in its structure, except for the partial surface oxidation, and most of the O was involved in the amorphous phase. In order words, as-synthesized CoP HNS exhibits hybrid crystalline–amorphous phase, and each region is composed of crystalline CoP and amorphous Co–O–P phase, respectively.

It is unusual to construct a crystalline–amorphous hybrid phase in a single particle. Therefore, the formation mechanism of this unique hybrid architecture in CoP HNS/CF was investigated, which is depicted in Fig. 3(e). As $Co_2(OH)_2CO_3$ NS precursor is heat-treated in inert atmosphere, it shows a weight loss over 250 °C due to a removal of hydroxyl and carbonate ions (TGA in Fig. S9 in the ESM) [30, 31], indicating that precursor becomes to cobalt oxide above 250 °C. Simultaneously, the precursor was reacted with a P source and topochemically converted to amorphous Co–O–P throughout the sheet. As the phosphidation reaction proceeded, crystalline CoP began to form from the edge of the amorphous Co–O–P. Then, the Co element inside the sheet gradually diffused to the edge with the accompaniment of increasing crystalline CoP by the Kirkendall effect [32, 33]. Indeed, more Co was detected in crystalline CoP by TEM-EDS line-scanning (Fig. 3(d)). However, the confined phosphidation time inhibited further outward diffusion of Co and inward diffusion of P, resulting in the formation of a unique hybrid crystalline–amorphous phase. However, it is estimated that more crystalline CoP was formed in CoP HNS/CF when phosphorized for 12 h, which was identified in XPS spectra (Figs. 2(f) and 2(g)) and TEM analysis (Fig. S10 in the ESM). Also, TEM EDS elemental mapping analysis showed that as phophidation time was increased, the P ratio in CoP HNS was also increased and the O ratio was decreased (Table S1 in the ESM). This phenomenon, the formation of crystalline–amorphous hybrid phase, can also be observed after the phosphidation of crystalline Co_3O_4 NS, where crystalline Co_3O_4 was converted to amorphous Co–O–P, and then crystalline CoP was formed from the edge (Fig. S11 in the ESM). This unique architecture significantly contributed to the superb electrocatalytic HER performance, as mentioned below.

The electrocatalytic HER performance of CoP HNS/CF was evaluated in acidic (0.5 M H_2SO_4), neutral (0.5 M PBS), and alkaline (1 M KOH) media in a three-electrode cell configuration, along with the performance of benchmark Pt(20 wt.%)/C and CoP NW/CF for comparison. All the potentials were corrected with iR compensation (the *R* values corresponding to each polarization curve are shown in Table S2 in the ESM) and converted to the RHE potential. At first, the electrocatalytic HER performance of all samples in acidic and neutral media was investigated. Figure 4(a) presents the polarization curves of CoP HNS/CF, CoP NW/CF, and Pt/C by LSV in an acidic medium. The bare CF substrate exhibited negligible current density within the investigated potential range, indicating no electrocatalytic activity of CF. Impressively, CoP HNS/CF only required a small overpotential of 48 mV to achieve a current density of −10 $mA \cdot cm^{-2}$ in the acidic medium, which is comparable to that of Pt/C (30 mV) and better than those of the

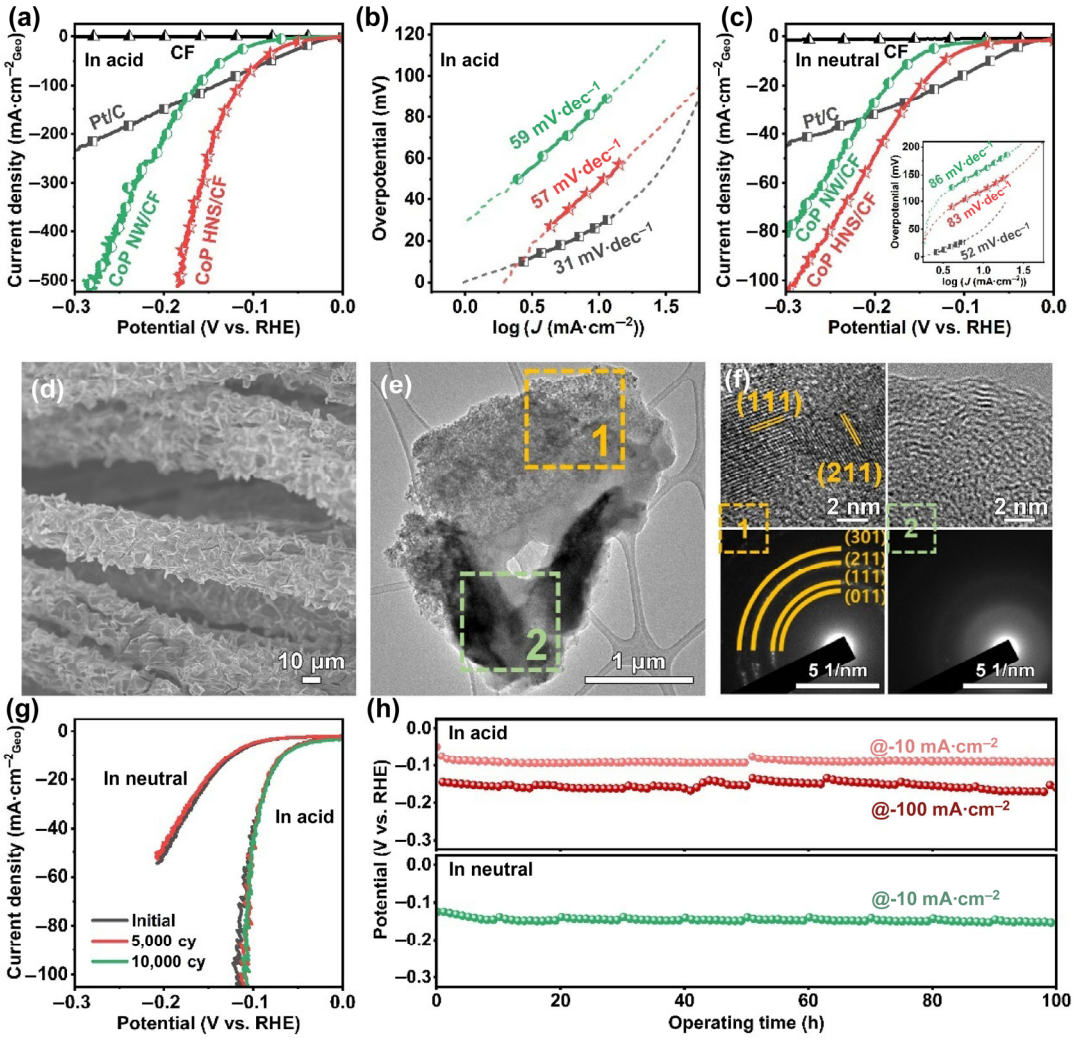

Figure 4 Electrocatalytic HER performance of CoP HNS/CF in acidic and neutral media. (a) Polarization curves measured in 0.5 M H_2SO_4 and (b) Tafel plots derived from (a). (c) Polarization curves measured in 0.5 M PBS and Tafel plots. (d) SEM and (e) TEM images after HER test in 0.5 M H_2SO_4. (f) SAED patterns taken from sections 1 and 2 in (e). (g) Polarization curves after the 1st, 5,000th, and 10,000th CV in 0.5 M H_2SO_4, 0.5 M PBS. (h) Chronopotentiometric curves in 0.5 M H_2SO_4, 0.5 M PBS.

recently reported cobalt phosphide-based HER electrocatalyst (Table S3 in the ESM). Moreover, CoP HNS/CF required lower overpotential than Pt/C to achieve higher current densities. CoP HNS/CF exhibited an overpotential of 115 mV at a current density of −100 mA·cm^{-2}, which was lower than that of Pt/C (133 mV). Even at a high current density of −500 mA·cm^{-2}, CoP HNS/CF still required an overpotential of only 180 mV. In addition, the Tafel slope of CoP HNS/CF derived from the polarization curve was estimated to be 57 mV·dec^{-1} (Fig. 4(b)), which indicates that CoP HNS/CF follows the Volmer–Heyrovsky HER mechanism and electrochemical desorption of hydrogen is rate-determining step [10, 34].

CoP HNS/CF also exhibited much higher HER activity than CoP NW/CF, with approximately 4 times higher double-layer capacitance (C_{dl}) than CoP NW/CF (Figs. S12(a)–S12(c) in the ESM). By calculating ECSA from C_{dl}, polarization curves of CoP HNS/CF and CoP NW/CF were normalized to the ECSA (Fig. S12(d) in the ESM). Interestingly, both CoP HNS/CF and CoP NW/CF showed similar curves in all potential ranges. In addition, CoP NW/CF exhibited a similar Tafel slope (59 mV·dec^{-1}) to CoP HNS/CF (Fig. 4(b)). Considering these results, CoP HNS/CF and CoP NW/CF had the same intrinsic electrocatalytic HER activity and kinetics in the acidic medium. In other words, a closely packed but separated ultrathin sheet-type architecture can provide many more electrocatalytic reactive sites than the wire-type architecture per unit substrate area, demonstrating the superiority of the CoP HNS architecture for the high- performance HER electrocatalyst. Meanwhile, CoP HNS/CF phosphorized for 12 h had smaller C_{dl} (25.7 mF·cm^{-2}) than CoP HNS/CF treated for 1 h (Fig. S13 in the ESM), possibly due to the same agglomeration in the process of phosphidation, which resulted in inferior HER performance.

It is worth noting that the CoP HNS/CF showed high HER performance in the neutral medium as well. In light of HER activity, CoP HNS/CF showed a similar tendency to that measured in the acidic medium. CoP HNS/CF showed the overpotential of 120 mV at a current density of −10 mA·cm^{-2}, which is comparable to those of the recently reported cobalt phosphide-based HER electrocatalyst (Table S4 in the ESM).

CoP HNS/CF displayed higher HER activity at high current densities than Pt/C as well as CoP NW/CF (Fig. 4(c)). The Tafel slopes of CoP HNS/CF and CoP NW/CF were estimated to be 83 and 86 mV·dec^{-1}, respectively (inset of Fig. 4(c)), indicating that both follow the same HER mechanism. We further investigated the catalytic properties by electrochemical impedance spectroscopy (EIS) in acidic and neutral media. Figure S14 in the ESM shows the Nyquist plots of CoP NW/CF and CoP HNS/CF and their fitting data are summarized in Table S5 in the ESM. CoP HNS/CF had lower charge

transfer resistances (R_{ct}) than CoP NW/CF in acidic and neutral media, implying that CoP HNS/CF would exhibit higher charge transfer kinetic properties in acidic and neutral media.

The microstructural and surface chemical changes of the CoP HNS/CF after HER test in acidic medium were evaluated. Figures 4(d)–4(f) show the SEM and TEM analysis of CoP HNS/CF after chronopotentiometric test at a current density of −10 mA·cm^{-2} for 10 h. As shown in the SEM image, CoP HNS was still well attached on the surface of CF and maintained its initial 2D sheet shape (Fig. 4(d)). TEM image and SAED patterns show that there still existed two distinct regions corresponding to the crystalline and amorphous parts (Figs. 4(e) and 4(f)). No significant changes in the crystal were found in the XRD pattern after the HER test (Fig. S15 in the ESM), confirming that the original architecture of CoP HNS/CF remained after the HER test in the acidic medium. In addition, CoP HNS/CF did not show significant changes in morphology and crystal structure after the HER test in a neutral medium (Fig. S16 in the ESM), which also confirms the high structural stability of the CoP HNS/CF in neutral medium.

The long-term durability and steady-state electrocatalytic activity of the CoP HNS/CF were evaluated by cyclic voltammetry (CV) and chronopotentiometry test in acidic and neutral media. Figure 4(g) shows the polarization curves of CoP HNS/CF after the 1st, 5,000th, and 10,000th CV cycles at a scan rate of 100 mV·s^{-1} (each CV profile is shown in Figs. S17(a) and S17(b) in the ESM). Compared with the initial state, a negligible shift in the polarization curves was observed after the 5,000th cycle in both the acidic and neutral media, and even after the 10,000th in acidic media. As shown in chronopotentiometry curves (Fig. 4(h)), there was negligible degradation in the overpotentials during the chronopotentiometric test at a constant current density of −10 mA·cm^{-2} for 100 h in acidic and neutral media. Furthermore, the polarization curves showed negligible differences before and after the chronopotentiometric test (Figs. S17(c) and S17(d) in the ESM). Furthermore, CoP HNS/CF also exhibited a stable potential curve, even at a high current density of −100 mA·cm^{-2}, demonstrating the superior stability of CoP HNS/CF in acidic medium.

Next, the electrocatalytic HER performance of CoP HNS/CF in alkaline medium was evaluated. Figures 5(a) and 5(b) present the polarization curves of CoP HNS/CF, CoP NW/CF and Pt/C in alkaline medium, and their Tafel plots derived from the polarization curves. The overpotentials and Tafel slopes for Pt/C and CoP HNS/CF in acidic and alkaline media are compared in Fig. 5(c). In the alkaline medium, CoP HNS/CF exhibited overpotentials of 55 and 119 mV to achieve current densities of −10 and −100 mA·cm^{-2}, respectively, and a Tafel slope of 50 mV·dec^{-1}, which are much better than those of recently reported cobalt phosphide-based HER electrocatalyst (Table S6 in the ESM). It is known that most HER electrocatalysts, including Pt, show inferior catalytic activity

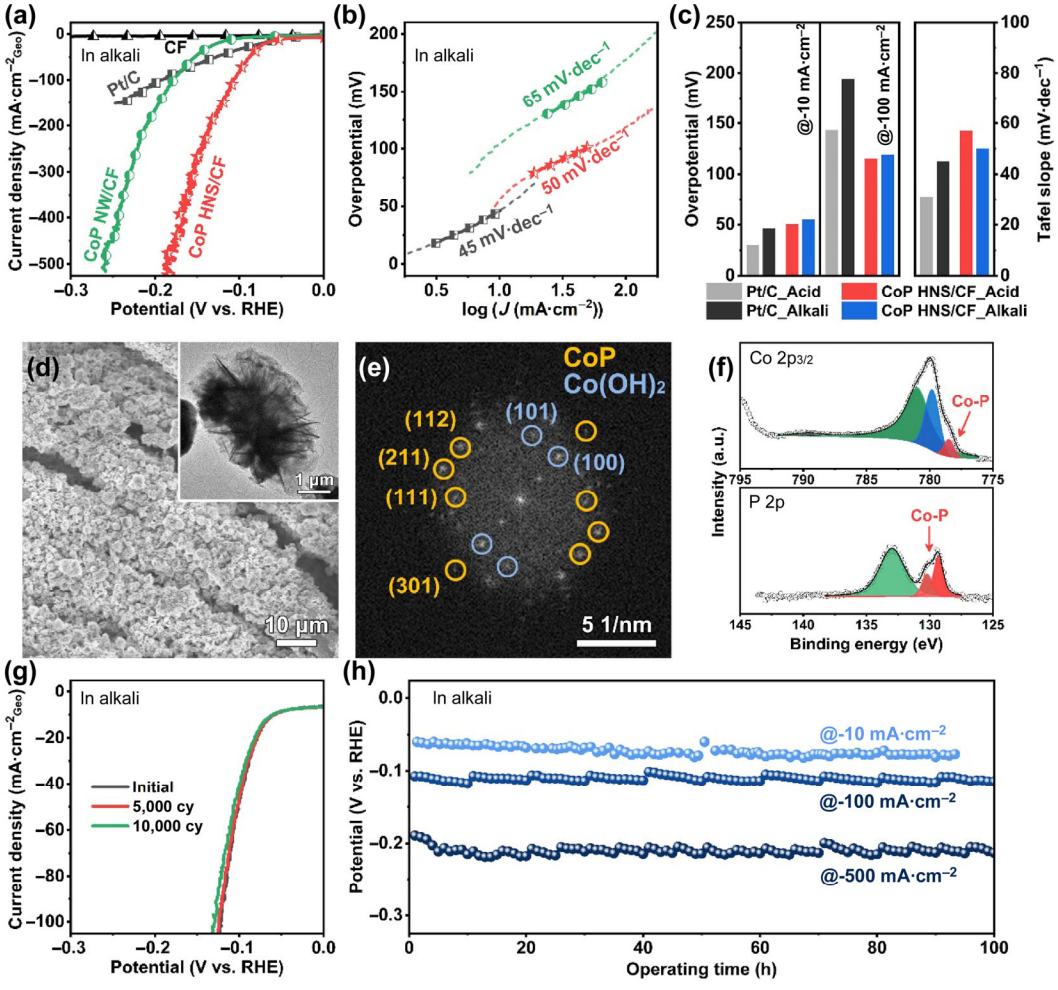

Figure 5 Electrocatalytic HER performance of CoP HNS/CF in alkaline medium. (a) Polarization curves measured in 1 M KOH and (b) Tafel plots derived from (a). (c) Comparison in overpotentials and Tafel slopes for Pt/C and CoP HNS/CF measured in 0.5 M H_2SO_4 and 1 M KOH. (d) SEM, TEM images and (e) corresponding FFT patterns, (f) Co 2p$_{3/2}$ and P 2p XPS spectra after HER test in 1 M KOH. (g) Polarization curves after the 1st, 5,000th, and 10,000th CV in 1 M KOH. (h) Chronopotentiometric curves in 1 M KOH.

and kinetics in alkaline media than in acidic media due to the scarcity of proton donors, and thus, an additional water dissociation process in the Volmer reaction is crucial for HER in alkaline media [1, 2, 10, 35]. Shown in Fig. 5(c), Pt/C showed much higher overpotentials and Tafel slope in the alkaline medium. However, CoP HNS/CF exhibited similar overpotentials at the same current density, and an even lower Tafel slope in alkaline medium compared to those measured in acidic medium. In addition, CoP HNS/CF outperformed the electrocatalytic activity of Pt/C over −0.06 V (vs. RHE). In addition, CoP HNS/CF exhibited the lower R_{ct} than CoP NW/CF in alkaline medium (Fig. S14 and Table S5 in the ESM), implying that CoP HNS/CF would exhibit higher charge transfer kinetic properties in all pH conditions.

In order to find out this outstanding HER performance in alkaline medium, we explored the conditions of CoP HNS/CF after HER test in alkaline medium. Figure 5(d) shows the SEM and TEM images of CoP HNS/CF after HER test in alkaline medium. Unexpectedly, CoP HNS/CF showed a morphological change from a sheet shape to a flower-like form. The fast Fourier transform (FFT) patterns for inset of Fig. 5(d) revealed that crystalline $Co(OH)_2$ as well as CoP were detected in the flower-like particle (Fig. 5(e)). In the XPS spectra, the core-level peaks at 778.5 eV in Co $2p_{3/2}$ and 129.3/130.2 eV in P 2p corresponding to the characterization peak of CoP binding were still observed (Fig. 5(f)). Also, CoP as well as $Co(OH)_2$ were detected in the XRD pattern (Fig. S18 in the ESM). So, it is suggested that both the phase and morphological reorganization occurred after HER in alkaline medium. Also, it is known that oxophilic sites, such as oxide and hydroxide, exhibit a strong affinity toward water molecules, which accelerates the water dissociation and promotes the formation of adsorbed protons (H_{ads}) in the Volmer reaction step [35–37]. Thus, the formation of $Co(OH)_2$ during the HER had a positive effect on the HER performance in alkaline medium. In short, by controlling the crystalline and amorphous phases in CoP HNS/CF in the phosphidation process, we optimized the reorganization and formation of the CoP/$Co(OH)_2$ interface HER in the alkaline medium. Moreover, the synergistic effect between CoP and $Co(OH)_2$ enabled the implementation of outstanding electrocatalytic performance in the alkaline medium.

CoP HNS/CF also exhibited the high durability and stability in alkaline medium. After the continuous CV test for the 10,000th cycle (each CV profile is shown in Fig. S19(a) in the ESM), a negligible shift of the polarization curves was observed in alkaline medium (Fig. 5(g)). There was also negligible degradation in the HER performance during the chronopotentiometric test at constant current densities of −10 and −100 mA·cm^{-2} for 100 h in alkaline medium (Fig. 5(h) and Fig. S19(b) in the ESM), because the catalysts were still tightly attached to the CF substrate after the HER test (Fig. 5(d)). For practical use in the water electrolyzer systems, the ability to endure the high current for a long period is critical [16, 17, 38]. In light of this, CoP HNS/CF showed exceptional prolonged durability for 100 h at a high current density of 500 mA·cm^{-2} (Fig. 5(h)).

Finally, we examined the possibility of large-scale manufacturing of CoP HNS/CF. For this, CoP HNS/CF with a size (4 cm × 4 cm) was fabricated in the same synthetic process. After each hydrothermal reaction and phosphidation step, the color of the reaction area was changed uniformly (Fig. 6(a)). As shown in the SEM images and XRD pattern of 4-end-point, CoP HNS was uniformly supported on CF (Fig. 6(b) and Fig. S20 in the ESM). The electrocatalytic HER performance of the large-areal CoP HNS/CF was evaluated in acidic and alkaline media. As shown in the polarization curves (Fig. 6(c)), large-areal CoP HNS/CF operated a similar electrocatalytic activity both in acidic and alkaline media, which exhibited overpotentials of 69/72 and 130/127 mV at current densities of −10 and −100 mA·cm^{-2} in acidic/alkaline media, respectively. Furthermore, multi-step chronopotentiometry ranging from −10 to −100 mA·cm^{-2} with an increment of −10 mA·cm^{-2} per

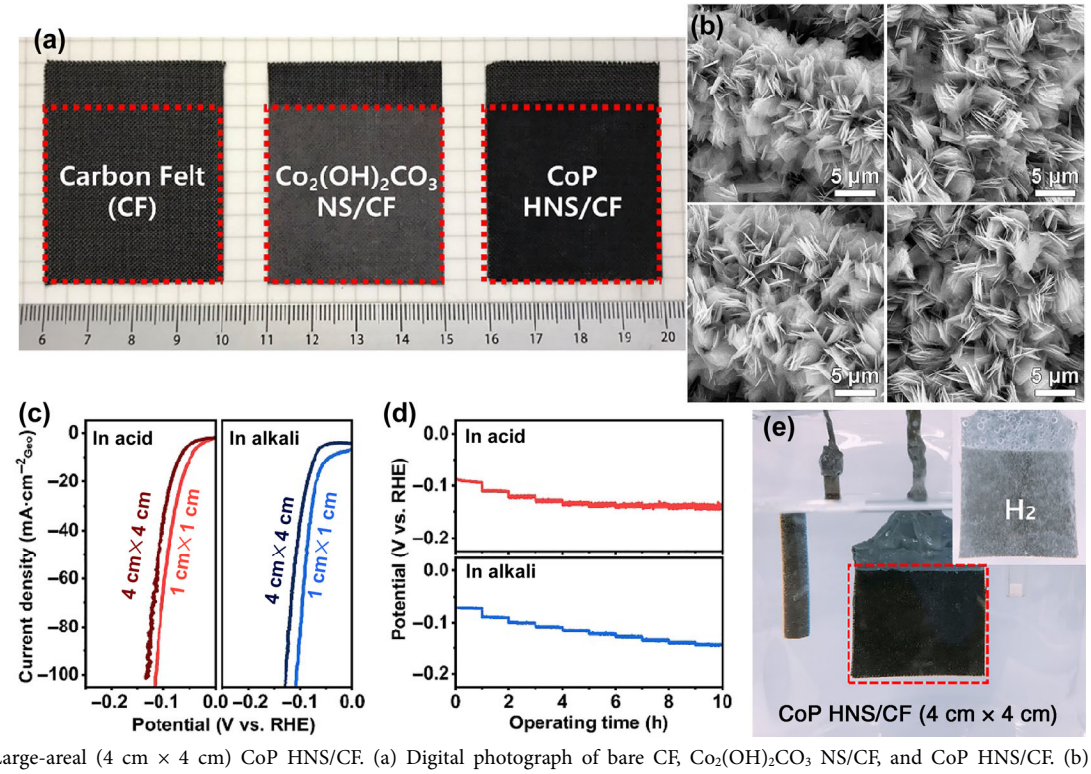

Figure 6 Large-areal (4 cm × 4 cm) CoP HNS/CF. (a) Digital photograph of bare CF, $Co_2(OH)_2CO_3$ NS/CF, and CoP HNS/CF. (b) SEM images corresponding to 4-end-point of CoP HNS/CF in (a). (c) Polarization curves and (d) multi-step chronopotentiometric tests in 0.5 M H_2SO_4 and 1 M KOH. (e) Digital photograph of CoP HNS/CF with HER operation.

hour was evaluated. At the start of −10 mA·cm^{-2}, the potential immediately leveled off at −88 and −72 mV (vs. RHE) in acidic and alkaline media, respectively, and remained stable for the subsequent hour. It also showed stable potential curves in the following steps, as well as plenty of hydrogen bubbles in all steps (Figs. 6(d) and 6(e) and Movie ESM1), confirming the high electrocatalytic activity of large-areal CoP HNS/CF. Thus, it is demonstrated that the fabrication method in this work can be universally applied in practical production.

4 Conclusions

In summary, we developed a novel CoP HNS/CF electrocatalyst via hydrothermal and subsequent thermal phosphidation process; this catalyst exhibited superior electrocatalytic HER performance in a wide pH range. An ultrathin, close-packed $Co_2(OH)_2CO_3$ NS precursor was successfully constructed on the CF substrate during hydrothermal reaction. Moreover, a crystalline–amorphous hybrid phase in a single NS was induced by controlling the phosphidation time. Benefiting from an abundant exposure of electrochemically reactive sites originating from a unique architecture, it exhibited a superior electrocatalytic HER performance with low overpotentials and Tafel slopes in a wide pH range. In particular, phase and morphological reorganization in CoP HNS/CF resulted in the outstanding electrocatalytic performance in alkaline medium. Due to its high structural stability, CoP HNS/CF exhibited high stability and durability; this was true even at high current densities (500 mA·cm^{-2}) for over 100 h operation. In addition, the synthetic strategy of CoP HNS/CF can be employed easily to fabricate a large-scale CoP HNS/CF electrode, which also shows comparable electrocatalytic activity and stability to those of small CoP HNS/CF. Considering its high electrocatalytic HER activity that outperforms commercial Pt/C, high stability in universal-pH, and ease of scaling up, this novel electrocatalyst fabricated in this study is a potential material for meeting the demand for a robust, highly active, stable, and cost-effective HER electrocatalyst.

Acknowledgements

This work is supported by the National Research Foundation of Korea (NRF) Grant funded by the Ministry of Science and ICT, South Korea (No. 2016M3A7B4909318). We thank the Korea Basic Science Institute (KBSI) for the technical support. Microstructural images were obtained using a Hitachi SU-70 scanning electron microscope at the KBSI.

Electronic Supplementary Material: Supplementary material (additional XRD, SEM, XPS, thermogravimetric analysis, TEM, electrochemical analysis, and comparison of HER performance) is available in the online version of this article at https://doi.org/10.1007/s12274-020-2881-y.

References

[1] Tian, J. Q.; Liu, Q.; Asiri, A. M.; Sun, X. P. Self-supported nanoporous cobalt phosphide nanowire arrays: An efficient 3D hydrogen-evolving cathode over the wide range of pH 0–14. *J. Am. Chem. Soc.* **2014**, *136*, 7587–7590.

[2] Zhai, M. K.; Wang, F.; Du, H. B. Transition-metal phosphide-carbon nanosheet composites derived from two-dimensional metal-organic frameworks for highly efficient electrocatalytic water-splitting. *ACS Appl. Mater. Interfaces* **2017**, *9*, 40171–40179.

[3] Wu, K. L.; Chen, Z.; Cheong, W. C.; Liu, S. J.; Zhu, W.; Cao, X.; Sun, K. A.; Lin, Y.; Zheng, L. R.; Yan, W. S. et al. Toward bifunctional overall water splitting electrocatalyst: General preparation of transition metal phosphide nanoparticles decorated N-doped porous carbon spheres. *ACS Appl. Mater. Interfaces* **2018**, *10*, 44201–44208.

[4] Song, H. J.; Yoon, H.; Ju, B.; Lee, G. H.; Kim, D. W. 3D architectures of quaternary Co-Ni-S-P/graphene hybrids as highly active and stable bifunctional electrocatalysts for overall water splitting. *Adv. Energy Mater.* **2018**, *8*, 1802319.

[5] Tabassum, H.; Guo, W. S.; Meng, W.; Mahmood, A.; Zhao, R.; Wang, Q. F.; Zou, R. Q. Metal-organic frameworks derived cobalt phosphide architecture encapsulated into B/N Co-doped graphene nanotubes for all pH value electrochemical hydrogen evolution. *Adv. Energy Mater.* **2017**, *7*, 1601671.

[6] Wang, X. D.; Xu, Y. F.; Rao, H. S.; Xu, W. F.; Chen, H. Y.; Zhang, W. X.; Kuang, D. B.; Su, C. Y. Novel porous molybdenum tungsten phosphide hybrid nanosheets on carbon cloth for efficient hydrogen evolution. *Energy Environ. Sci.* **2016**, *9*, 1468–1475.

[7] Guha, A.; Vineesh, T. V.; Sekar, A.; Narayanaru, S.; Sahoo, M.; Nayak, S.; Chakraborty, S.; Narayanan, T. N. Mechanistic insight into enhanced hydrogen evolution reaction activity of ultrathin hexagonal boron nitride-modified Pt electrodes. *ACS Catal.* **2018**, *8*, 6636–6644.

[8] Huang, J. W.; Li, Y. R.; Xia, Y. F.; Zhu, J. T.; Yi, Q. H.; Wang, H.; Xiong, J.; Sun, Y. H.; Zou, G. F. Flexible cobalt phosphide network electrocatalyst for hydrogen evolution at all pH values. *Nano Res.* **2017**, *10*, 1010–1020.

[9] Yu, J.; Zhong, Y. J.; Wu, X. H.; Sunarso, J.; Ni, M.; Zhou, W.; Shao, Z. P. Bifunctionality from synergy: CoP nanoparticles embedded in amorphous CoO_x nanoplates with heterostructures for highly efficient water electrolysis. *Adv. Sci.* **2018**, *5*, 1800514.

[10] Xu, K.; Cheng, H.; Lv, H. F.; Wang, J. Y.; Liu, L. Q.; Liu, S.; Wu, X. J.; Chu, W. S.; Wu, C. Z.; Xie, Y. Controllable surface reorganization engineering on cobalt phosphide nanowire arrays for efficient alkaline hydrogen evolution reaction. *Adv. Mater.* **2018**, *30*, 1703322.

[11] Cao, H. S.; Xie, Y.; Wang, H. L.; Xiao, F.; Wu, A. P.; Li, L.; Xu, Z. K.; Xiong, N.; Pan, K. Flower-like CoP microballs assembled with (002) facet nanowires via precursor route: Efficient electrocatalysts for hydrogen and oxygen evolution. *Electrochim. Acta* **2018**, *259*, 830–840.

[12] Pu, Z. H.; Liu, Q.; Asiri, A. M.; Sun, X. P. Tungsten phosphide nanorod arrays directly grown on carbon cloth: A highly efficient and stable hydrogen evolution cathode at all pH values. *ACS Appl. Mater. Interfaces* **2014**, *6*, 21874–21879.

[13] Kibsgaard, J.; Tsai, C.; Chan, K.; Benck, J. D.; Nørskov, J. K.; Abild-Pedersen, F.; Jaramillo, T. F. Designing an improved transition metal phosphide catalyst for hydrogen evolution using experimental and theoretical trends. *Energy Environ. Sci.* **2015**, *8*, 3022–3029.

[14] Laursen, A. B.; Patraju, K. R.; Whitaker, M. J.; Retuerto, M.; Sarkar, T.; Yao, N.; Ramanujachary, K. V.; Greenblatt, M.; Dismukes, G. C. Nanocrystalline Ni_5P_4: A hydrogen evolution electrocatalyst of exceptional efficiency in both alkaline and acidic media. *Energy Environ. Sci.* **2015**, *8*, 1027–1034.

[15] Shi, Y. M.; Zhang, B. Recent advances in transition metal phosphide nanomaterials: Synthesis and applications in hydrogen evolution reaction. *Chem. Soc. Rev.* **2016**, *45*, 1529–1541.

[16] Wang, J.; Xu, F.; Jin, H. Y.; Chen, Y. Q.; Wang, Y. Non-noble metal-based carbon composites in hydrogen evolution reaction: Fundamentals to applications. *Adv. Mater.* **2017**, *29*, 1605838.

[17] Yu, X. W.; Zhang, M.; Tong, Y.; Li, C.; Shi, G. Q. A large-scale graphene-bimetal film electrode with an ultrahigh mass catalytic activity for durable water splitting. *Adv. Energy Mater.* **2018**, *8*, 1800403.

[18] Kibsgaard, J.; Jaramillo, T. F. Molybdenum phosphosulfide: An active, acid-stable, earth-abundant catalyst for the hydrogen evolution reaction. *Angew. Chem., Int. Ed.* **2014**, *53*, 14433–14437.

[19] Zhuo, J. Q.; Cabán-Acevedo, M.; Liang, H. F.; Samad, L.; Ding, Q.; Fu, Y. P.; Li, M. X.; Jin, S. High-performance electrocatalysis for hydrogen evolution reaction using Se-doped pyrite-phase nickel diphosphide nanostructures. *ACS Catal.* **2015**, *5*, 6355–6361.

[20] Jin, Z. Y.; Li, P. P.; Huang, X.; Zeng, G. F.; Jin, Y.; Zheng, B. Z.; Xiao, D. Three-dimensional amorphous tungsten-doped nickel phosphide microsphere as an efficient electrocatalyst for hydrogen evolution. *J. Mater. Chem. A* **2014**, *2*, 18593–18599.

[21] Mahmood, J.; Li, F.; Jung, S. M.; Okyay, M. S.; Ahmad, I.; Kim, S.

J.; Park, N.; Jeong, H. Y.; Baek, J. B. An efficient and pH-universal ruthenium-based catalyst for the hydrogen evolution reaction. *Nat. Nanotechnol*. **2017**, *12*, 441–446.

[22] Zhao, G. Q.; Lin, Y.; Rui, K.; Zhou, Q.; Chen, Y. P.; Dou, S. X.; Sun, W. P. Epitaxial growth of $Ni(OH)_2$ nanoclusters on MoS_2 nanosheets for enhanced alkaline hydrogen evolution reaction. *Nanoscale* **2018**, *10*, 19074–19081.

[23] Hao, G. Q.; Rui, K.; Dou, S. X.; Sun, W. P. Heterostructures for electrochemical hydrogen evolution reaction: A review. *Adv. Funct. Mater*. **2018**, *28*, 1803291.

[24] Xu, W. W.; Lu, Z. Y.; Wan, P. B.; Kuang, Y.; Sun, X. M. High-performance water electrolysis system with double nanostructured superaerophobic electrodes. *Small* **2016**, *12*, 2492–2498.

[25] Ren, B. W.; Li, D. Q.; Jin, Q. Y.; Cui, H.; Wang, C. X. *In-situ* tailoring cobalt nickel molybdenum oxide components for overall water-splitting at high current densities. *ChemElectroChem* **2019**, *6*, 413–420.

[26] Che, Q. J.; Li, Q.; Tan, Y.; Chen, X. H.; Xu, X.; Chen, Y. S. One-step controllable synthesis of amorphous $(Ni\text{-}Fe)S_x/NiFe(OH)_y$ hollow microtube/sphere films as superior bifunctional electrocatalysts for quasi-industrial water splitting at large-current-density. *Appl. Catal. B: Environ*. **2019**, *246*, 337–348.

[27] Xu, R.; Wu, R.; Shi, Y. M.; Zhang, J. F.; Zhang, B. Ni_3Se_2 nanoforest/ Ni foam as a hydrophilic, metallic, and self-supported bifunctional electrocatalyst for both H_2 and O_2 generations. *Nano Energy* **2016**, *24*, 103–110.

[28] Masikhwa, T. M.; Dangbegnon, J. K.; Bello, A.; Madito, M. J.; Momodu, D.; Barzegar, F.; Manyala, N. Effect of growth time of hydrothermally grown cobalt hydroxide carbonate on its super-capacitive performance. *J. Phys. Chem. Solids* **2016**, *94*, 17–24.

[29] Wang, J. K.; Gao, R.; Zheng, L. R.; Chen, Z. J.; Wu, Z. H.; Sun, L. M.; Hu, Z. B.; Liu, X. F. CoO/CoP heterostructured nanosheets with an O–P interpenetrated interface as a bifunctional electrocatalyst for Na–O_2 battery. *ACS Catal*. **2018**, *8*, 8953–8960.

[30] Li, B. X.; Xie, Y.; Wu, C. Z.; Li, Z. Q.; Zhang, J. Selective synthesis of cobalt hydroxide carbonate 3D architectures and their thermal conversion to cobalt spinel 3D superstructures. *Mater. Chem. Phys*. **2006**, *99*, 479–486.

[31] Wang, S. L.; Qian, L. Q.; Xu, H.; Lü, G. L.; Dong, W. J.; Tang, W. H. Synthesis and structural characterization of cobalt hydroxide carbonate nanorods and nanosheets. *J. Alloy Compd*. **2009**, *476*, 739–743.

[32] Anderson, B. D.; Tracy, J. B. Nanoparticle conversion chemistry: Kirkendall effect, galvanic exchange, and anion exchange. *Nanoscale* **2014**, *6*, 12195–12216.

[33] Wang, T. T.; Wu, L. Q.; Xu, X. B.; Sun, Y.; Wang, Y. Q.; Zhong, W.; Du, Y. W. An efficient Co_3S_4/CoP hybrid catalyst for electrocatalytic hydrogen evolution. *Sci. Rep*. **2017**, *7*, 11891.

[34] Shinagawa, T.; Garcia-Esparza, A. T.; Takanabe, K. Insight on Tafel slopes from a microkinetic analysis of aqueous electrocatalysis for energy conversion. *Sci. Rep*. **2015**, *5*, 13801.

[35] Liu, T. T.; Liu, D. N.; Qu, F. L.; Wang, D. X.; Zhang, L.; Ge, R. X.; Hao, S.; Ma, Y. J.; Du, G.; Asiri, A. M. et al. Enhanced electrocatalysis for energy-efficient hydrogen production over CoP catalyst with nonelectroactive Zn as a promoter. *Adv. Energy Mater*. **2017**, *7*, 1700020.

[36] Xie, X. H.; Song, M.; Wang, L. G.; Engelhard, M. H.; Luo, L. L.; Miller, A.; Zhang, Y. Y.; Du, L.; Pan, H. L.; Nie, Z. M. et al. Electrocatalytic hydrogen evolution in neutral pH solutions: Dual-phase synergy. *ACS Catal*. **2019**, *9*, 8712–8718.

[37] Subbaraman, R.; Tripkovic, D.; Chang, K. C.; Strmcnik, D.; Paulikas, A. P.; Hirunsit, P.; Chan, M.; Greeley, J.; Stamenkovic, V.; Markovic, N. M. Trends in activity for the water electrolyser reactions on 3d M(Ni,Co,Fe,Mn) hydr(oxy)oxide catalysts. *Nat. Mater*. **2012**, *11*, 550–557.

[38] Zhou, H. Q.; Yu, F.; Zhu, Q.; Sun, J. Y.; Qin, F.; Yu, L.; Bao, J. M.; Yu, Y.; Chen, S.; Ren, Z. F. Water splitting by electrolysis at high current densities under 1.6 volts. *Energy Environ. Sci*. **2018**, *11*, 2858–2864.